PCCP
Physical Chemistry Chemical Physics

Accepted Manuscript

This article can be cited before page numbers have been issued, to do this please use: V. H. Ho, D. T. Ho, W. H. Shin and S. Y. Kim, *Phys. Chem. Chem. Phys.*, 2023, DOI: 10.1039/D2CP03275A.

ROYAL SOCIETY OF CHEMISTRY

rsc.li/pccp

Auxeticity of monolayer, few-layer, vdW heterostructure and ribbon penta-graphene

Viet Hung Ho[1], Duc Tam Ho[2], Won Ho Shin[1], Sung Youb Kim[1,*]

View Article Online
DOI: 10.1039/D2CP03275A

[1] Department of Mechanical Engineering, Ulsan National Institute of Science and Technology, Ulsan 44919, South Korea

[2] Department of Mechanical and Construction Engineering, Northumbria University, Newcastle upon Tyne NE1 8ST, United Kingdom

* Corresponding author, e-mail: sykim@unist.ac.kr

Using molecular statics simulations, we specially focus on investigating the negative Poisson's ratio of the monolayer, few-layer, van der Waals heterostructure, and ribbon penta-graphene. As a result, we provide evidence to show that the Poisson's ratio is the combination of bond stretching and angle rotating mechanism. The auxetic of monolayer penta-graphene is owned by the dominance of bond stretching. However, the significant effect of angle rotating mechanism causes the enhancement of in-plane Poisson's ratio of few-layer penta-graphene. Furthermore, the elongation of interlayer bonds results in a negative out-of-plane Poisson's ratio in few-layer penta-graphene. The strong dependence of Poisson's ratio on stacking configuration and number of layers was found. We also show that the van der Waals interaction slightly enhances the auxeticity of heterostructure penta-graphene. Finally, we discuss the significant effects of warped edges on the auxeticity of penta-graphene ribbons.

Keywords: negative Poisson's ratio, auxetics, penta-graphene, monolayer, few-layer, heterostructure, ribbon molecular statics simulations.

DOI: 10.1039/D2CP03275A

1. Introduction

Poisson's ratio is a fundamental property that quantifies the deformation of a material in transverse directions under the applied loading. Most materials typically have positive Poisson's ratios, which means that they contract when stretched. However, some materials, which are known as auxetic materials [1], have opposite behavior, i.e., they expand when stretched. Auxeticity is being investigated since the works of Lakes [2,3] and Wojciechowski [4,5]. Auxetic materials and structures show unique characteristics, such as enhancing shear modulus and fracture toughness [2,6], thus they can be key applications in many fields such as the aerospace engineering [7], textile fabrics industry [8], biomedical applications [9], and strain sensors [10]. Auxetics are found in various structures [11], including foam structures [2], re-entrant geometry [12,13], rotating rigid units [14], chiral structures[15], Miura-origami structures [16,17], and many others [18–23]. Different from bulk counterparts, metal nanoplates [24] and nanowires [25] are shown to exhibit a negative Poisson's ratio owing to the effects of surface stresses. In the recent decade, the search for two-dimensional (2D) materials with auxeticity has attracted lots of attention. The auxeticity in 2D materials have been obtained by introducing vacancy defects [26], cutting into periodic porous [27], creating rippling sheet [28–30], and patterning hydrogenation [31,32]. 2D materials, that do not have any external modification, can still have intrinsic auxeticity (for instance, graphene [33], black phosphorus [34–36], borophane [37], some 1T-MX_2 [38], δ-Phosphorene [39], bilayer graphane [40], and few others [41–43]). Ho *et al.* developed a design algorithm based on machine learning to optimize hydrogenated graphene structure with tunable auxeticity [44].

Penta-graphene (PG) is a new 2D carbon allotrope, which was discovered using first-principle calculation [45]. It is proven that it has mechanical stability and a quasi-direct band gap of approximately 3.25 eV [45–47]. The electronic properties of PG can be changed by stacking [48,49], chemical functionalization [50], doping [51], and introducing defects [52]. PG is a promising candidate for application in nanoelectronics [50,53], optical devices [46], batteries [54], and others [55,56]. Regarding the mechanical properties, monolayer PG has been shown to have high in-plane stiffness (264 GPa.nm) [45,57,58], which is approximately 80% of pristine graphene (340 N/m)[59]. At room temperature, the thermal conductivity of monolayer PG ranges from 167 [60] to 645 W/mK [61], which is much lower than that of pristine graphene (2000-5000 W/mK) [62]. So far, previous studies found that monolayer PG exhibits a negative in-plane Poisson's ratio [45,57,63], but the Poisson's ratio of few-layer PG, heterostructure

PG, and ribbon PG have not yet been investigated. Therefore, an understanding of the Poisson's ratio of other PG structures is necessary.

View Article Online
DOI: 10.1039/D2CP03275A

In this study, the Poisson's ratios of monolayer, ribbon, few-layer, and heterostructure PG are investigated. Poisson's ratio of structure is the interplay between bond stretching and angle rotating mechanism. For monolayer PG, we found that the bond stretching was dominant factor causing the negative in-plane Poisson's ratio. Meanwhile, for few-layer PG, in which the interlayer bonds are formed between layers, the angle rotation mechanism had a significant effect that increased the in-plane Poisson's ratio. Unlike monolayer PG, few-layer PG shows auxetic behavior along the out-of-plane direction due to the elongation of interlayer bonds. Moreover, we observed the effects of stacking configuration and number of layers on Poisson's ratio. We also studied effect of the van der Waals interactions on auxeticity of heterostructure PG. Finally, it was also demonstrated that the warped edge effect of the PG ribbon on Poisson's ratio.

2. Computational details

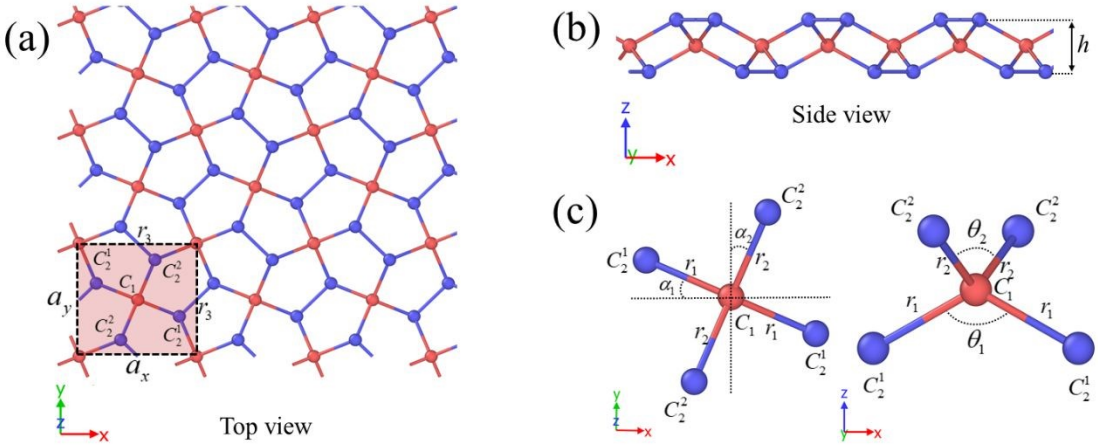

Fig. 1. (a) Top and (b) side view of the monolayer PG. C_1 (red) are carbon atoms with sp^3 hybridization. C_2^1 and C_2^2 are carbon atoms with sp^2 hybridization at the bottom and top layers, respectively. A unit cell is presented in a red shade. (c) Illustration of bonds (r_1 and r_2) and angles (θ_1, θ_2, α_1, and α_2).

DOI: 10.1039/D2CP03275A

Fig. 1 shows the structure of monolayer PG, which was confirmed to be stable in a previous study [45]. The size of this structure is 35.92 Å × 35.92 Å, which contains 600 carbon atoms. For simulations of monolayer and few-layer PG, periodic boundary conditions were applied in the *x*- and *y*-direction. Meanwhile, the Tersoff potential, parameterized by Erhart *et al*. [64], was used to describe the carbon-carbon atoms interaction. This potential can reproduce the values of the geometrical parameters and mechanical properties of PG with high accuracy. To investigate the Poisson's ratio of PG structures, molecular statics (MS) simulations were performed in the following steps. First, the structure was fully relaxed to obtain zero stress in all directions (unstrained configuration) using the conjugate gradient energy method [65]. The minimization was ended when the energy tolerance, which is defined as the ratio of energy variation between successive iterations to the energy magnitude, was 10^{-16} (unitless). After that, the uniaxial strain was applied with the strain increment of 0.001 in the *x*-direction, whereas the lengths of structure in other directions (*y*- and *z*-) were changed to maintain zero stresses. All simulations were conducted using LAMMPS [66], OVITO [67] was used for their visualization. Poisson's ratio is calculated as:

$$\nu_{xy} = -\frac{\partial \varepsilon_y}{\partial \varepsilon_x} \tag{1a}$$

$$\nu_{xz} = -\frac{\partial \varepsilon_z}{\partial \varepsilon_x} \tag{1b}$$

where ν_{xy} and ν_{xz} are the in-plane and the out-of-plane Poisson's ratios for the *x*-direction stretching, respectively, and ε_x, ε_y, and ε_z are strains in the *x*-, *y*-, and *z*-directions, respectively.

3. Results and discussions

3.1. Auxeticity of monolayer penta-graphene

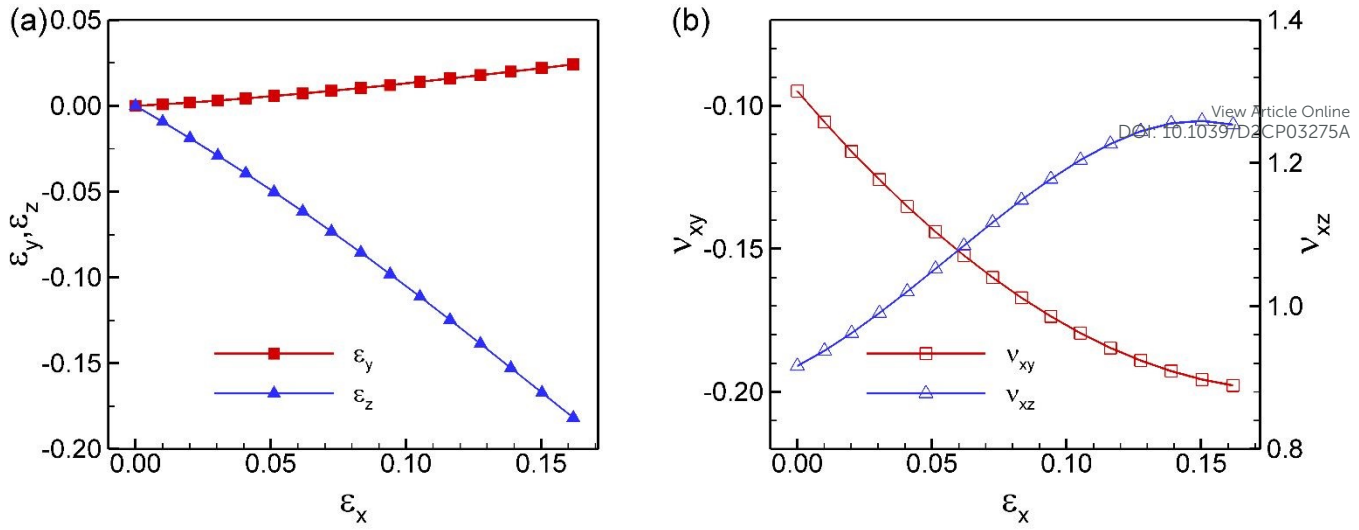

Fig.2. (a) Deformation of monolayer PG in the *y*- and *z*-direction with uniaxial stretching along the *x*-direction. Data were fitted polynomial functions $\varepsilon_{y,z} = a\varepsilon_x^4 + b\varepsilon_x^3 + c\varepsilon_x^2 + d\varepsilon_x$. The R-square value of both fitting functions are of 1.0. (b) The Poisson's ratio of PG which was obtained by Eq. 1.

In Fig. 2a, we present the resultant transverse strain in the *y*- (ε_y) and *z*-direction (ε_z) corresponding to the tensile deformation in the *x*-direction (ε_x). We observed the increase in ε_y, indicating the expansion of PG in the in-plane direction. The reduction in ε_z suggests contraction of the PG in the out-of-plane direction. The relationships between transverse strains (ε_y and ε_z) and applied strain ε_x were fitted to fourth-order polynomials $\varepsilon_{y,z} = a\varepsilon_x^4 + b\varepsilon_x^3 + c\varepsilon_x^2 + d\varepsilon_x$ with *a*, *b*, *c*, and *d* are fitting variables. For ε_y, $a = -0.24$, $b = -0.90$, $c = 0.55$, and $d = 0.085$; and for ε_z, $a = 29.87$, $b = -6.78$, $c = -0.96$, and $d = -0.92$; the goodness-of-fit R-squared values of both fitting functions are of 1.0. Then, these fitting variables were used for the estimation of ν_{xy} and ν_{xz} (using Eq. 1a and Eq. 1b). In the unstrained configuration, we obtained a negative in-plane Poisson's ratio of $\nu_{xy} = -0.085$, which is in good agreement with previous results [63] and a positive out-of-plane Poisson's ratio of $\nu_{xz} = 0.92$. As the monolayer PG is stretched, ν_{xy} becomes more negative, e.g., $\nu_{xy} = -0.19$ at $\varepsilon = 0.16$.

To demonstrate the origin of the negative Poisson's ratio in monolayer PG during the tensile deformation, we studied two deformation mechanisms: the bond stretching and the angle rotating mechanisms. The illustration of two deformation mechanisms is presented in Fig. S1 of the Supporting Information. The Poisson's ratio of PG is determined by the trade-off between these two deformation mechanisms. Previous studies had discussed the role of the bond stretching and angle rotating on Poisson's ratio of carbon nanotube [68], graphene [33], black phosphorus [35], and bilayer graphane [40]. In the case of PG, the Poisson's ratio corresponding to bond stretching and angle rotating mechanism can be simply expressed by algebra. The size of a unit cell in the *y*-direction and thickness (*z*-direction), which is displayed in a red shade in Fig. 1, is given as:

$$a_y = 2\left(r_1 \sin\frac{\theta_1}{2}\sin\alpha_1 + r_2 \sin\frac{\theta_2}{2}\cos\alpha_2 \right) \tag{2a}$$

$$h = r_1 \cos\frac{\theta_1}{2} + r_2 \cos\frac{\theta_2}{2} \tag{2b}$$

The transverse strains are calculated as:

$$\varepsilon_y = \frac{\Delta a_y}{a_y^0} = \frac{a_y - a_y^0}{a_y^0} = \frac{2\left(r_1 \sin\frac{\theta_1}{2}\sin\alpha_1 + r_2 \sin\frac{\theta_2}{2}\cos\alpha_2 \right)}{a_y^0} - 1 \tag{3a}$$

$$\varepsilon_z = \frac{\Delta h}{h^0} = \frac{h - h^0}{h^0} = \frac{r_1 \cos\frac{\theta_1}{2} + r_2 \cos\frac{\theta_2}{2}}{h^0} - 1 \tag{3b}$$

where a_y^0 and h^0 are the length of a unit cell in the *y*-direction and thickness of PG in the unstrained configuration, respectively.

Using Eq.1a, the in-plane Poisson's ratio is expressed as:

$$\nu_{xy} = -\frac{\partial \varepsilon_y}{\partial \varepsilon_x} = -\frac{2}{a_y^0}\left(A_1 \frac{\partial r_1}{\partial \varepsilon_x} + A_2 \frac{\partial r_2}{\partial \varepsilon_x} + A_3 \frac{\partial \theta_1}{\partial \varepsilon_x} + A_4 \frac{\partial \theta_2}{\partial \varepsilon_x} + A_5 \frac{\partial \alpha_1}{\partial \varepsilon_x} - A_6 \frac{\partial \alpha_2}{\partial \varepsilon_x} \right) \tag{4}$$

with $A_1 = \sin\frac{\theta_1}{2}\sin\alpha_1$, $A_2 = \sin\frac{\theta_2}{2}\cos\alpha_2$, $A_3 = \frac{1}{2}r_1\sin\alpha_1\cos\frac{\theta_1}{2}$, $A_4 = \frac{1}{2}r_2\cos\alpha_2\cos\frac{\theta_2}{2}$, $A_5 = r_1\sin\frac{\theta_1}{2}\cos\alpha_1$, and $A_6 = r_2\sin\frac{\theta_2}{2}\sin\alpha_2$.

View Article Online
DOI: 10.1039/D2CP03275A

As given in Eq. 4, ν_{xy} can be decomposed into six components, which present the dependence of bond lengths r_1, r_2, angles $\theta_1, \theta_2, \alpha_1$ and α_2 on applied strain ε_x. In particular, $\frac{\partial r_1}{\partial \varepsilon_x}$ and $\frac{\partial r_2}{\partial \varepsilon_x}$, which are strain dependence of r_1 and r_2; $\frac{\partial \theta_1}{\partial \varepsilon_x}$, $\frac{\partial \theta_2}{\partial \varepsilon_x}$, $\frac{\partial \alpha_1}{\partial \varepsilon_x}$ and $\frac{\partial \alpha_2}{\partial \varepsilon_x}$ which present strain dependence of angles $\theta_1, \theta_2, \alpha_1$ and α_2, respectively. In Fig. 3, we show variations in the bonds and angles as the monolayer PG is stretched in the *x*-direction. Regarding variations in bond lengths, we observed that r_1, r_2 and r_3 are elongated. However, as the tensile deformation is in the *x*-direction, the amount of increment of r_1 is approximately seven times larger than those of r_2 and r_3. The bond stretching mechanism leads to auxeticity in both the in-plane and out-of-plane directions. In terms of angles, angle θ_1 and angle θ_2 linearly increase, leading to an expansion in the in-plane direction, and a reduction in the thickness direction. Angle α_1, however, remarkably decreases; for example, at ε =0.16, value α_1 reduces approximately 16.4%. As shown in Eq. 4, a reduction in α_1 contributes to a positive Poisson's ratio. Meanwhile, the angle α_2 changes slightly, suggesting a minor contribution to the Poisson's ratio.

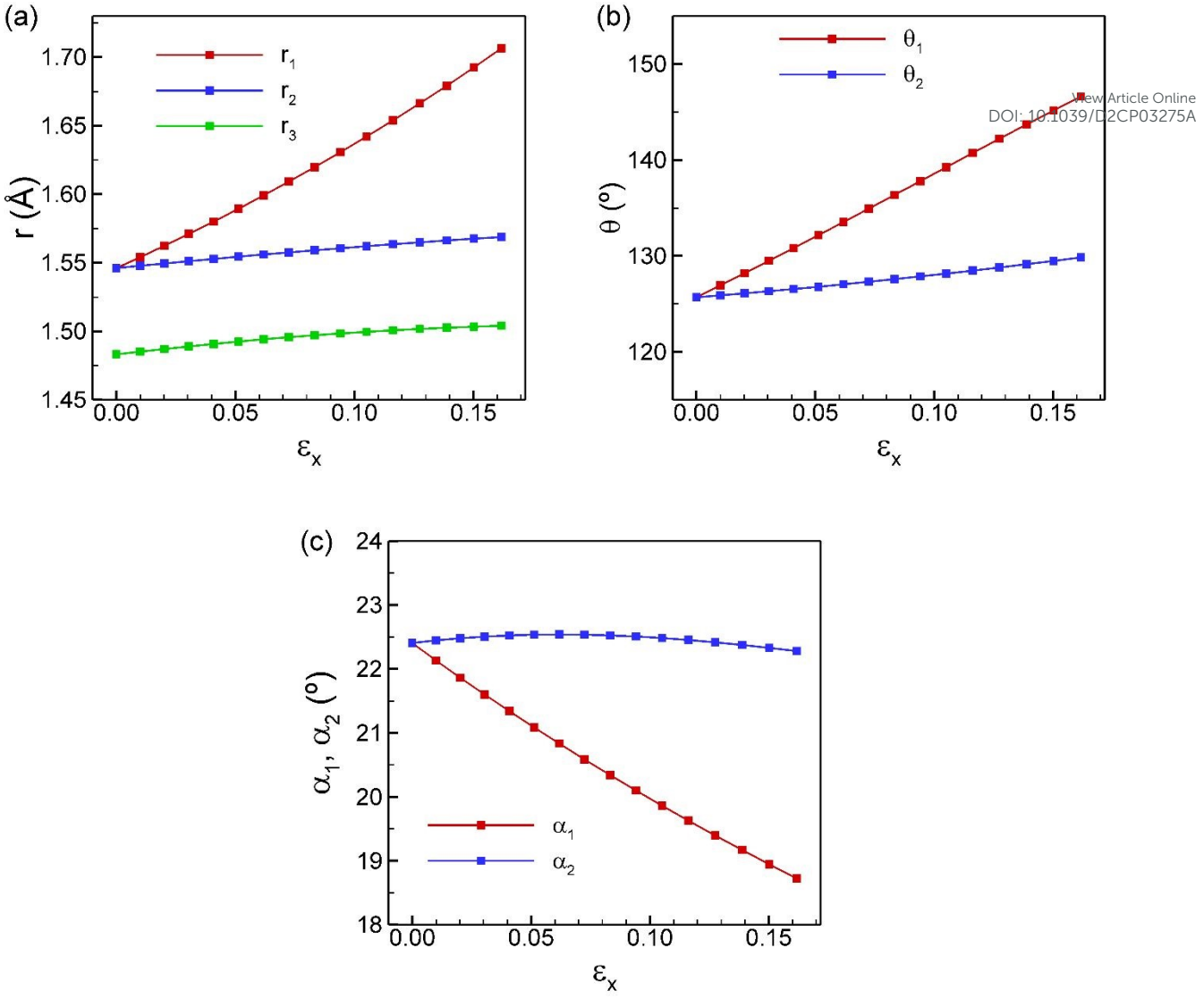

Fig. 3. The variation of bonds and angles as functions of applied strain. (a) bond lengths (r_1 , r_2, and r_3), (b) angles θ_1 , θ_2, and (c) angles α_1 and α_2.

To determine the effect of the bond and angle variation to Poisson's ratio, we performed a geometrical analysis on the strain dependence of ε_y and ε_z with two separate pathways. In the case of first pathway (PW1), we used Eq. 3 to calculate ε_y and ε_z, where the values of r_1 and r_2 are obtained from the simulations at each applied strain ε_x, and values of angles are obtained at $\varepsilon_x = 0$ ($\theta_1 = \theta_2$ =125.68º and $\alpha_1 = \alpha_2$ =22.41º). For the second pathway (PW2), Eq. (3) was also used, where values of bond lengths r_1 and r_2 are obtained at $\varepsilon_x = 0$ ($r_1 = r_2$ =1.546 Å), and the θ_1, θ_2, α_1 and α_2 are obtained from the simulation at each value of ε_x. Fig. 4 shows

View Article Online
DOI: 10.1039/D2CP03275A

the relationship between the resultant strains and applied strain corresponding to two pathways. It is clearly observed that if the deformation of PG follows PW1, both ε_y and ε_z increase. However, when the deformation of the PG follows PW2, both ε_y and ε_z decrease. For the in-plane deformation, the increment of ε_y, resulting from the PW1, is larger than that of reduction resulting from PW2. Thus, the combination of these two pathways (PW1 and PW2) leads to the expansion in the in-plane direction. In the case of ε_z, the flattening in the thickness direction owned by PW2 surpasses the contribution of PW1, leading to a reduction in the out-of-plane deformation of monolayer PG under tension. This analysis is in good agreement with the results shown in Fig. 2a (Fig. S2 in the Supporting Information).

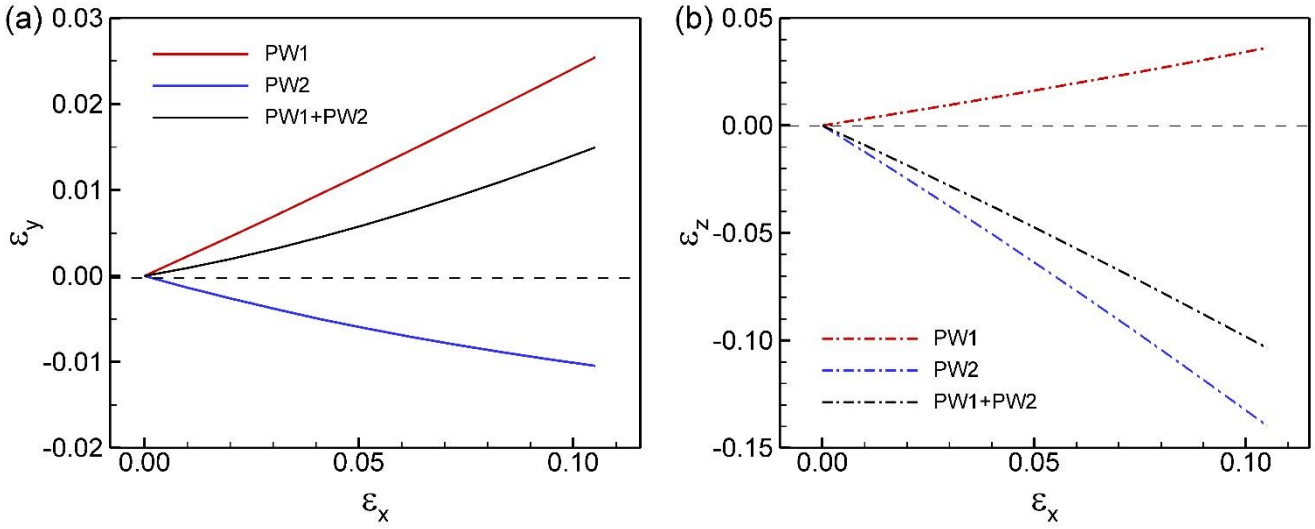

Fig. 4. (a) The strain along the in-plane and (b) out-of-plane direction of PG with PW1 and PW2.

Previous studies suggested that the negative in-plane Poisson's ratio of PG is the result of a flattening mechanism [57], which directly relates to the decrease in thickness of PG. Our results are in agreement with those of previous studies. It is worth noting that in the angle rotating mechanism, all angles including θ_1 and θ_2 are allowed to change. Even though θ_1 and θ_2 contribute to a negative Poisson's ratio, the overall combination of angles leads to the positive Poisson's ratio as shown in Fig. 4a. Zhang *et al.* [45] explained the in-plane auxeticity of PG as a consequence of rotation of the sp^2-hybridized atom. In particular, C_2^1 atoms

move along the tensile direction, resulting in a clockwise rotation of the $C_2^1C_1C_2^1$ plane. Consequently, the $C_2^2C_1C_2^2$ plane rotates in the same direction, resulting in the expansion of PG in the lateral direction. From the simulation results, α_1 decreases and α_2 increases (Fig. 3c), implying that $C_2^1C_1C_2^1$ plane and $C_2^2C_1C_2^2$ plane moved in two opposite directions, which is different from the suggested plane rotation mechanism.

For the free-standing monolayer graphene, thermal fluctuation may induce ripples owing to its low bending stiffness. The mechanical properties of graphene, such as thermal expansion [69] and bending rigidity [70], can be effected by the temperature and size of structure. To investigate the temperature and model size effects on Poisson's ratio of PG, we further examined the PG structures with larger size of 179.62 Å×179.62 Å and 359.23 Å × 359.23 Å, containing 15000 and 60000 atoms, respectively. The molecular dynamic (MD) simulations were performed at various temperatures ranging from 1 to 500 K. The results show that the values of ε_y are almost identical for all the structures (Fig. S3 in the Supporting Information). Similar results are obtained at different temperatures. This indicates that the effects of the model size and temperature on Poisson's ratio of PG can be neglected.

3.2. Auxetics of few-layer penta-graphene

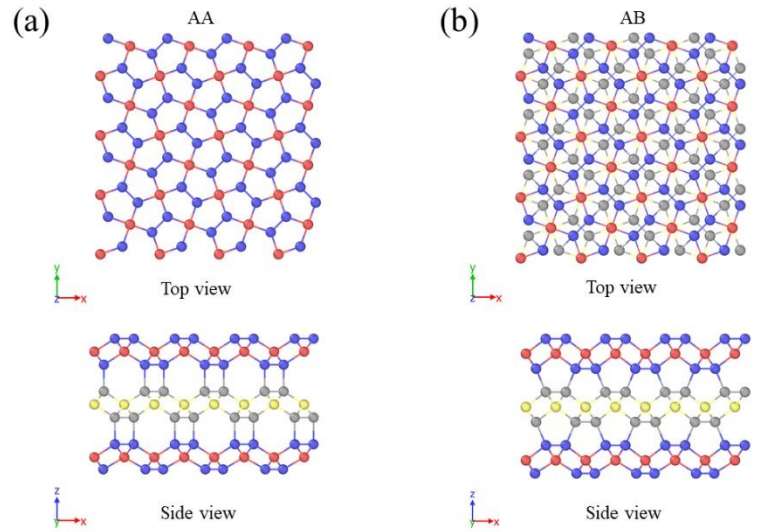

Fig. 5. Top view and side view of few-layer PG with (a) AA and (b) AB stacking configuration.

Previous studies focused on the electrical properties of few-layer penta-graphene [48,49]. In this section, we demonstrate the effect of the stacking configuration and number of layers on both in-plane and out-of-plane Poisson's ratios of few-layer PG. Fig. 5 shows PG structures with AA and AB stacking configurations, which can be fabricated by exfoliating the T12-carbon (T12C) phase while maintaining its dynamic stability [45]. In few-layer PG, C_2 atoms at interfaces form interlayer bonds changing the hybridizations of these C_2 atoms from sp^2 to sp^3, whereas C_2 atoms at the bottom and top of the slab remain sp^2 hybridization. In the case of bulk structures, all C_2 atoms at interfaces form interlayer bonds, resulting in a sp^3 hybridization for all the carbon atoms. The geometrical parameters and binding energies of monolayer, bilayer, and bulk PG with AA and AB stacking configurations are listed in Table 1. We define the bulk structure containing AA and AB stacking PG as AA-T12C and AB-T12C, respectively. The binding energy of a few-layer PG can be obtained from:

$$E_{binding} = \frac{\left(E_{nPG} - nE_{PG}\right)}{(n-1)A_i} \tag{5}$$

where E_{nPG} is the total energy of few-layer PG with n layers, and E_{PG} is the total energy of monolayer PG. A_i is the area of interface between layers.

Table 1. Calculated lattice constants a, height h, interlayer distances d, average energy per atom E_{ave} and binding energy of monolayer $E_{binding}$ of bilayer and bulk T12C with AA and AB stacking configuration.

	a (Å)	h (Å)	d (Å)	E_{ave} (eV/atom)	$E_{binding}$ (eV/A^2)
Monolayer	3.592	1.411		−6.451	
AA bilayer	3.575	1.490	1.590	−6.606	−0.145
AB bilayer	3.479	1.608	1.346	−6.768	−0.314
AA-T12C	3.565	1.554	1.590	−6.772	−0.152
AB-T12C	3.405	1.729	1.348	−7.153	−0.363

It can be observed that PG with AB stacking has lower values of E_{ave} and $E_{binding}$ compared to those with the AA stacking configuration. $E_{binding}$ of AB stacking configurations are approximately two times lower than that of AA stacking, thus PG structures with AB stacking configuration are more energetically favorable than those with AA stacking. Additionally, for both cases of stacking, E_{ave} and $E_{binding}$ decrease and approach the value of T12C with an increase in the number of layers, suggesting the stability of PG structure is related with n (Fig. S4 in the Supporting Information).

Fig. 6 shows the transverse strain ε_y versus the applied strain ε_x of few-layer PG with different numbers of layers. For both the AA and AB stacking configurations, a significant change in ε_y with the number of layers is demonstrated, implying a significant effect of n on the in-plane Poisson's ratio. In the case of AA bilayer PG, ε_y gradually increases as the structure is stretched (Fig. 6a). With $n \geq 4$, however, ε_y decreases and approaches a robust valley point, which is defined as the critical strain ε_c. This indicates that Poisson's ratio turns from a positive to a negative value at ε_c.

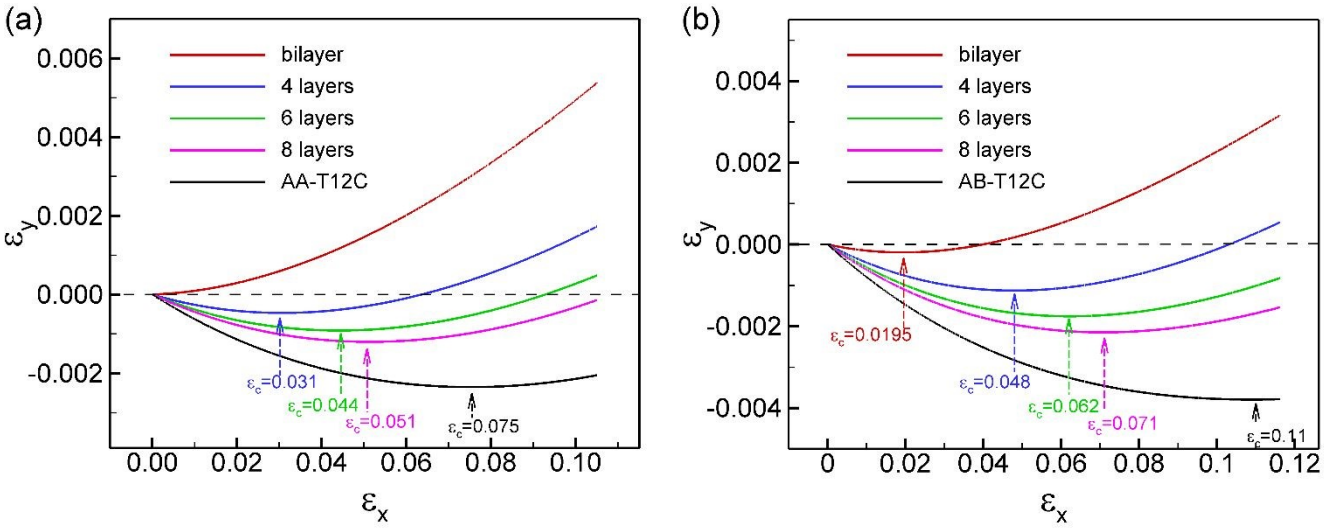

Fig. 6. The resultant strain in the *y*- direction as functions of applied strain in the *x*-direction of few-layer PG with (a) AA and (b) AB stacking configuration.

View Article Online
DOI: 10.1039/D2CP03275A

Fig. 7a shows the dependence of the in-plane Poisson's ratio on the number of layers. ν_{xy} of few-layer PG with AB and AA stacking configurations change from negative to positive values at n = 2 and 3, respectively. As the number of layers increases, ν_{xy} of few-layer PG approaches the value of bulk T12C, which are 0.068 and 0.086 for AA- and AB-T12C, respectively. We also found that with the same number of layers, ν_{xy} of AA stacking is lower than that of AB stacking. When the number of layers increases, the structure could be separated into two parts: (*i*) layers on the surface of structure, which contain atom with sp^2 hybridization, and (*ii*) layers in the interior part. The deformation of the surface layer is closed to that of monolayer PG, whereas the deformation of interior part is similar to that of bulk PG. Therefore, we can estimate the effective Poisson's ratio (ν_{eff}) of the few-layer PG as:

$$\nu_{eff} = \frac{\nu_0 + (n-1)\nu_{T12C}}{n} \quad (6)$$

where n is the number of layers; ν_0 and ν_{T12C} are the in-plane Poisson's ratio of monolayer PG (−0.085) and bulk T12C (0.068 for AA and 0.086 for AB stacking configuration), respectively. Fig. 7a shows that ν_{eff}, estimated using Eq. 6, is consistent with the results obtained from MS simulations. Similar to the tendency of ν_{xy}, we also found that the critical strain ε_c increases with n (Fig. 7b) and approaches the ε_c of the bulk, which are 0.076 and 0.11 for AA and AB stacking configuration, respectively. Fig.7 reveals that the dependence of the in-plane Poisson's ratio on the number of layers is larger in the case of AB stacking than that of AA stacking configuration.

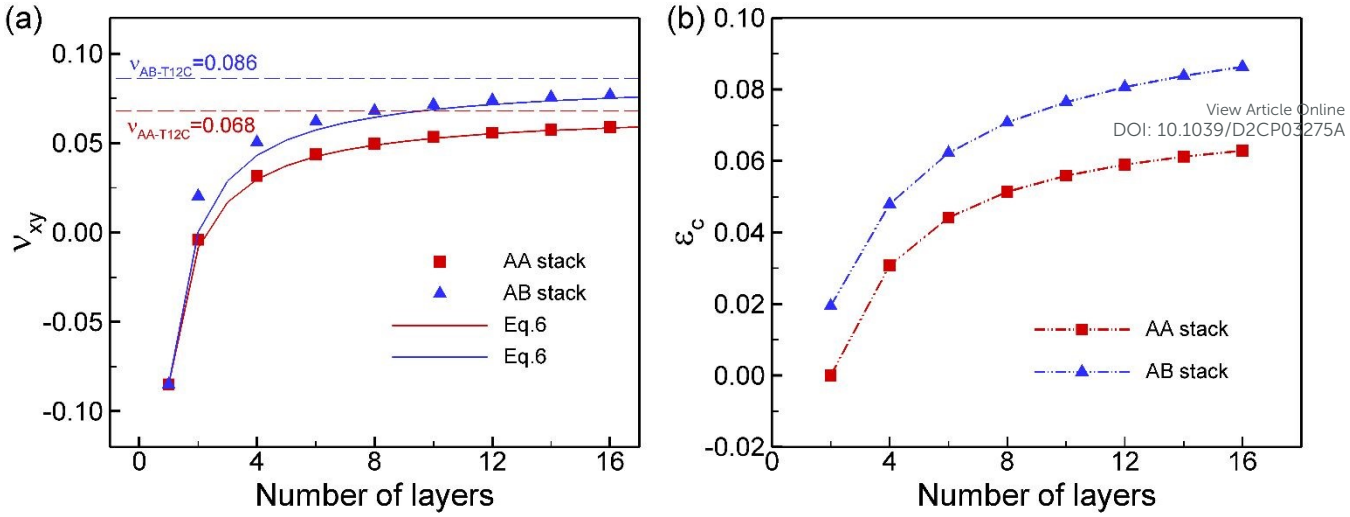

Fig. 7. (a) In-plane Poisson's ratio and (b) critical strain ε_c of few-layers PG with AA (red) and AB (blue) stacking configuration.

To better understand the effects of stacking on the in-plane Poisson's ratio of few-layer PG, we further investigated the deformation of AA- and AB-T12C under tension. In both cases of AA- and AB-T12C, r_1 and r_2 increase as the structure is stretched (Fig. S5 in the Supporting Information). Thus, the positive value of ν_{xy} may be originated from the dominance of the angle rotating mechanism. Fig. 8a shows that the increase in α_2 and reduction in α_1 increase during tension. It should be noted that in the case of monolayer PG, α_2 slightly changes, whereas α_2 of AA- and AB-T12C notably increases. The magnitude of $\Delta\alpha_2$ follows the order of AB-T12C > AA-T12C > monolayer. Consequently, we also found that ν_{xy} follows the order AB-T12C (0.086) > AA-T12C (0.068) > monolayer (−0.085). The increment in α_2 can be affected by the elongation of bond r_3 between C_2-C_2 atoms, as displayed in Fig. 8c. More specifically, we observed a remarkable difference between Δr_3 of bulk T12C and monolayer PG (Fig. 8b). For example, Δr_3 of AA- and AB-T12C are three and eight times higher, respectively, than that of monolayer PG. The difference in elongation of bond r_3 is due to the naturally stronger sp^2-sp^2 bonding of C_2-C_2 in monolayer PG compared to the sp^3-sp^3 bonding in bulk T12C. The large change in Δr_3 in bulk T12C leads to significant increment of α_2, especially in the case of AA-T12C. Therefore, a positive in-plane Poisson's ratios are obtained for both AA-

and AB-T12C. Moreover, we also investigated the out-of-plane Poisson's ratio of few-layer PG. As shown in Fig. S5, we found that ν_{xz} of AB-T12C decreases from 0.089 at $\varepsilon = 0$ to zero value at $\varepsilon = 0.117$. With $\varepsilon >$ 0.117, the value of ν_{xz} becomes negative, indicating the out-of-plane auxeticity. We also revealed that as shown in Fig. S6 (Supporting Information), the out-of-plane Poisson's ratio of few-layer PG decreases as the number of layer increases.

View Article Online
DOI: 10.1039/D2CP03275A

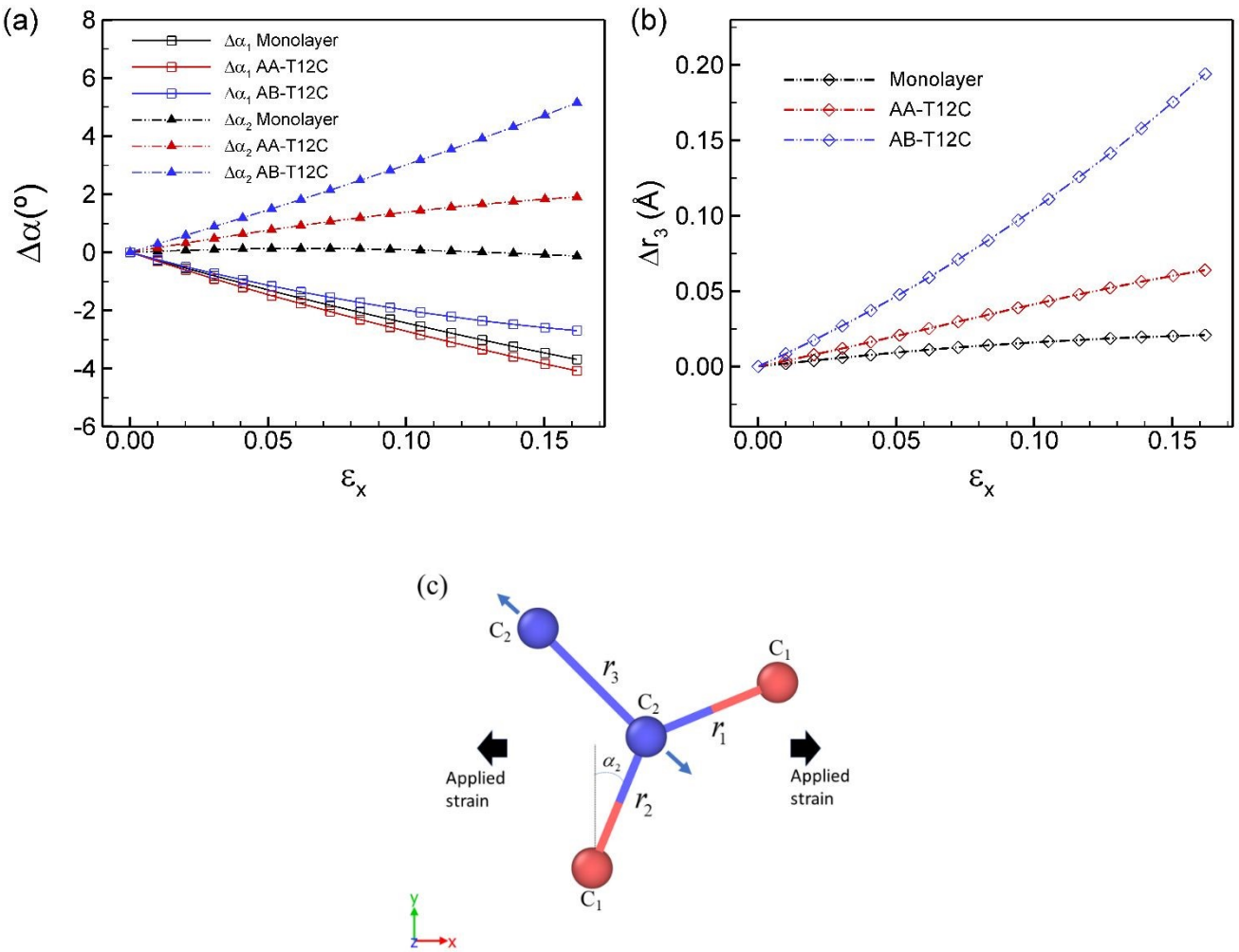

Fig. 8. (a) Variation of α_1, α_2 as the structure is stretched and (b) r_3 of AA- and AB-T12C as functions of applied strain. (c) Illustration of deformation of bond r_3 under stretching in the *x*-direction.

3.3. Auxetic of van der Waals heterostructures penta-graphene

View Article Online
DOI: 10.1039/D2CP03275A

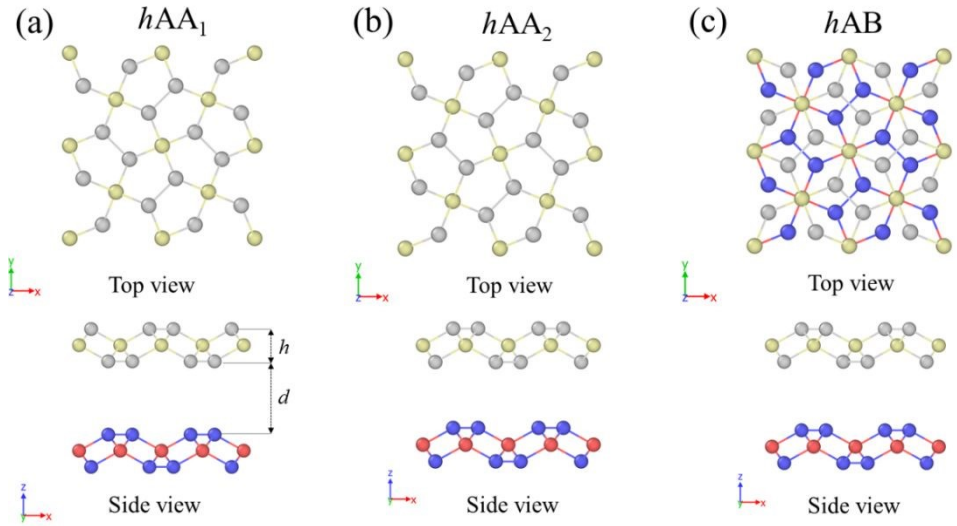

Fig. 9. Top and side views of PG heterostructures. (a) hAA$_1$, (b) hAA$_2$, and (c) hAB stacking. d and h are interlayer distance and height of PG, respectively.

Next, we study the Poisson's ratio of heterostructure PG for various stacking configurations. As shown in Fig.9, three different stacking configurations, which are hAA$_1$, hAA$_2$, and hAB, were evaluated. These three configurations were examined in study of heterostructure of PG and penta-BN$_2$ [71]. To describe the van der Waals (vdW) interactions between carbon atoms, the standard 12-6 Lennard-Jones potential was used: $V_{LJ} = 4\varepsilon\left[\left(\frac{\sigma}{r}\right)^{12} - \left(\frac{\sigma}{r}\right)^{6}\right]$, where r is the interatomic distance, and two potential parameters are $\varepsilon = 0.002635$ eV and σ = 3.369 Å [72]. The cut-off distance was set at 10 Å. Table 2 presents the calculated values of geometrical parameters and energy for stacking configurations of the bilayers and bulk heterostructures. It can be seen that E_{ave}, $E_{binding}$ and d of hAA$_2$ PG are smaller than those of hAA$_1$ and hAB PG. For instance, $E_{binding}$ of bilayer hAA$_1$, hAA$_2$, and hAB are −9.974 meV/A^2, −13.835 meV/A^2, and −12.084 meV/A^2, respectively. The dependence of binding energies of the bilayer heterostructure PG on interlayer distance is presented in Fig. S7 (Supporting Information). Therefore, among three stacking configurations, hAA$_2$ has the highest stability in terms of energy. Furthermore, it is also observed the structural transition of hAA$_1$ and hAB stack

configurations as the structure is stretched (Fig. S8 in the Supporting Information). Owing to the structural transition, the distance between layers varies from 3.193 Å to 2.917 Å for hAA$_1$ PG, and from 2.953 Å to 2.917 Å for hAB PG. Consequently, due to its higher stability, the heterostructure PG with hAA$_2$ stacking configuration is considered the dominant configuration.

Table 2. Calculated lattice constants a, height h, interlayer distances d, average energy per atom E_{ave} and binding energy of monolayer $E_{binding}$ of bilayer and bulk heterostructure PG with hAA$_1$, hAA$_2$ and hAB stacking configuration.

	a (Å)	h (Å)	d (Å)	E_{ave} (eV/atom)	$E_{binding}$ (meV/A^2)
Bilayer hAA$_1$	3.592	1.410	3.193	-6.461	-9.974
Bilayer hAA$_2$	3.593	1.409	2.766	-6.466	-13.835
Bilayer hAB	3.592	1.409	2.953	-6.464	-12.084
Bulk hAA$_2$	3.593	1.407	2.766	-6.481	-13.841

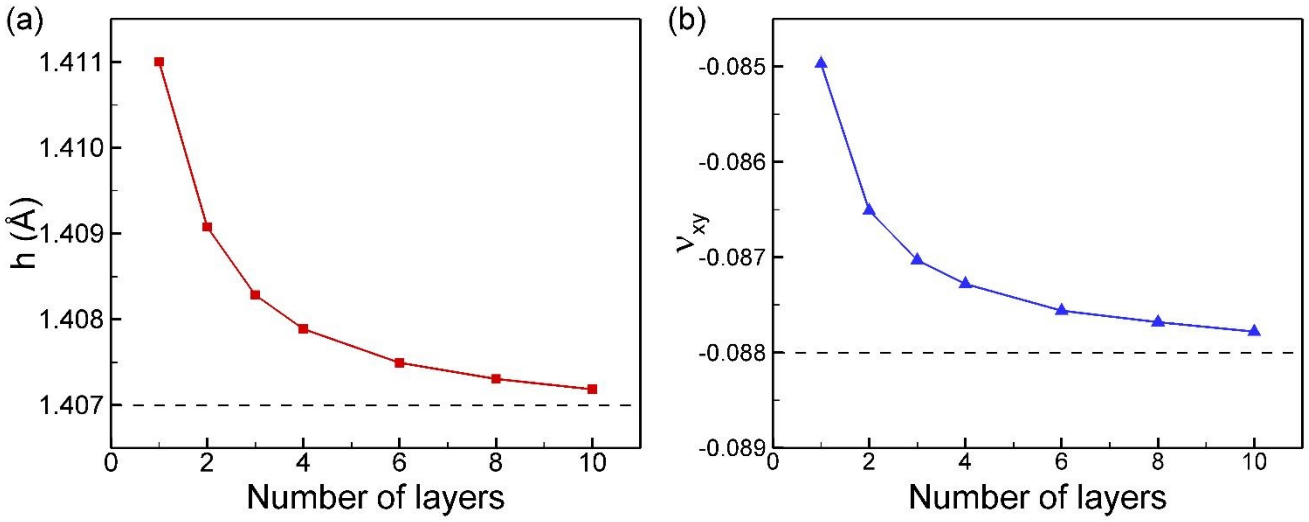

Fig. 10. (a) The average height of a PG layer in few-layer hAA$_2$ PG. (b) In-plane Poisson's ratio of few-layer hAA$_2$ PG. The black line demonstrates the value of bulk hAA$_2$ PG which is equal to −0.088.

The relationship between the in-plane Poisson's ratio of few-layer hAA$_2$ PG and the number of layers is shown in Fig. 10b. We found that the auxeticity enhances as the number of layers increases. ν_{xy} decreases slightly from −0.085, calculated for monolayer PG, to −0.088 calculated for bulk hAA$_2$ PG. This tendency is opposite to that found in the case of few-layers PG, in which the effect of interlayer bonding significantly increased ν_{xy}. However, the C_2 atoms in heterostructure PG do not form interlayer bonds and remain sp^2 hybridization; thus, the deformation of heterostructure PG tends to be similar to that of monolayer PG. As shown in Fig. 10a, the height of each layer in few-layer hAA$_2$ decreases as the number of layers increases. This indicates that in comparison with monolayer PG, each layer in heterostructure PG is compressed in the thickness (z-) direction owing to the vdW interactions. As the strain is applied, this compression enhances the fattening in thickness direction, resulting in the more negative in-plane Poisson's ratio in few-layer hAA$_2$ PG. While an experiment for stretching a heterostructure PG might be challenging due to the weak vdW interaction between the layers, we note that experimental measurement of Poisson's ratio of heterostructure black phosphorus was done by using four-point bending apparatus [36]. We expect that the method in previous study can be applied for studying heterostructure PG.

3.4. Auxeticity of penta-graphene ribbon

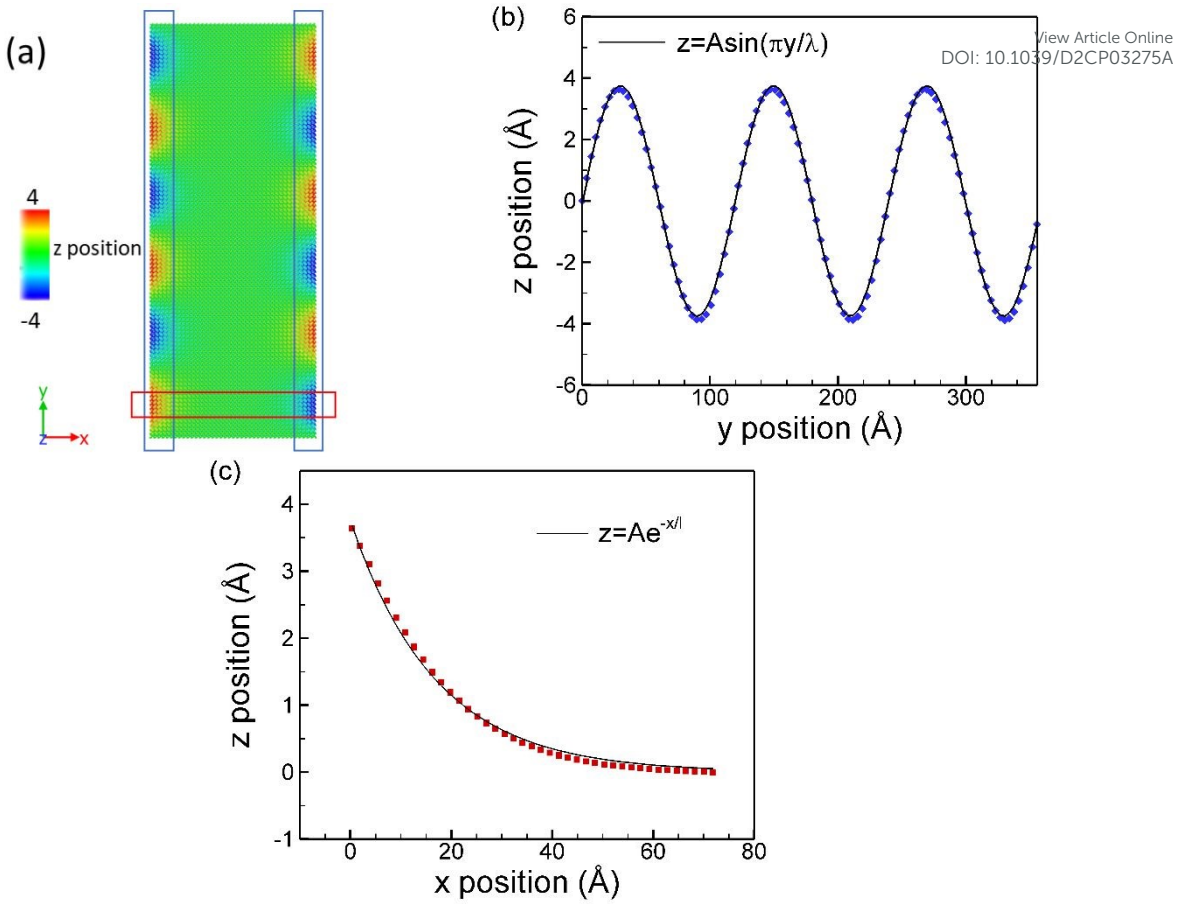

Fig. 11. (a) Configuration of PG ribbon with size of 143.69 Å × 359.23 Å with the number of warps n = 6. The periodic boundary condition is applied in the y-direction. The warped edge is described by function $s(x, y) = Ae^{-x/l}\sin(\pi y / \lambda)$. The position of atoms in the z-coordinate in the (b) y-direction and (c) x-direction.

For materials at the nanoscale, the surface and edge have significant effects on the mechanical properties of materials. We further investigated the edge effect on the in-plane Poisson's ratio of PG ribbons. Previous studies on 2D materials ribbon found that the edge stress induces out-of-plane buckling along the free edge, which can be warping, twisting, or curling [73–75]. The surface function $s(x, y) = Ae^{-x/l}\sin(\pi y / \lambda)$ is used to describe the structure of the warped edge [73]. Here, A is the amplitude of perturbation, l is the penetration depth, and λ is the half wavelength, and $\lambda = L / n$ with L is the length of PG ribbon and n is the number of warps. We discussed the relationship between the characteristics of the warped edge and wavelength in the Supporting Information. Fig. 11a illustrates the configuration of warped edge PG ribbon which has size of

143.69 Å × 359.23 Å with warping number n = 6 and λ=59.86 Å, which is found to be stable. The fitting parameters for the warped edges equal to 3.65 Å and 16.32 Å for warping amplitude (A) and penetration depth (l), respectively. The amplitude of ripples reaches the highest values along the free edges and decays along the width of the ribbon (Fig. 11c).

View Article Online
DOI: 10.1039/D2CP03275A

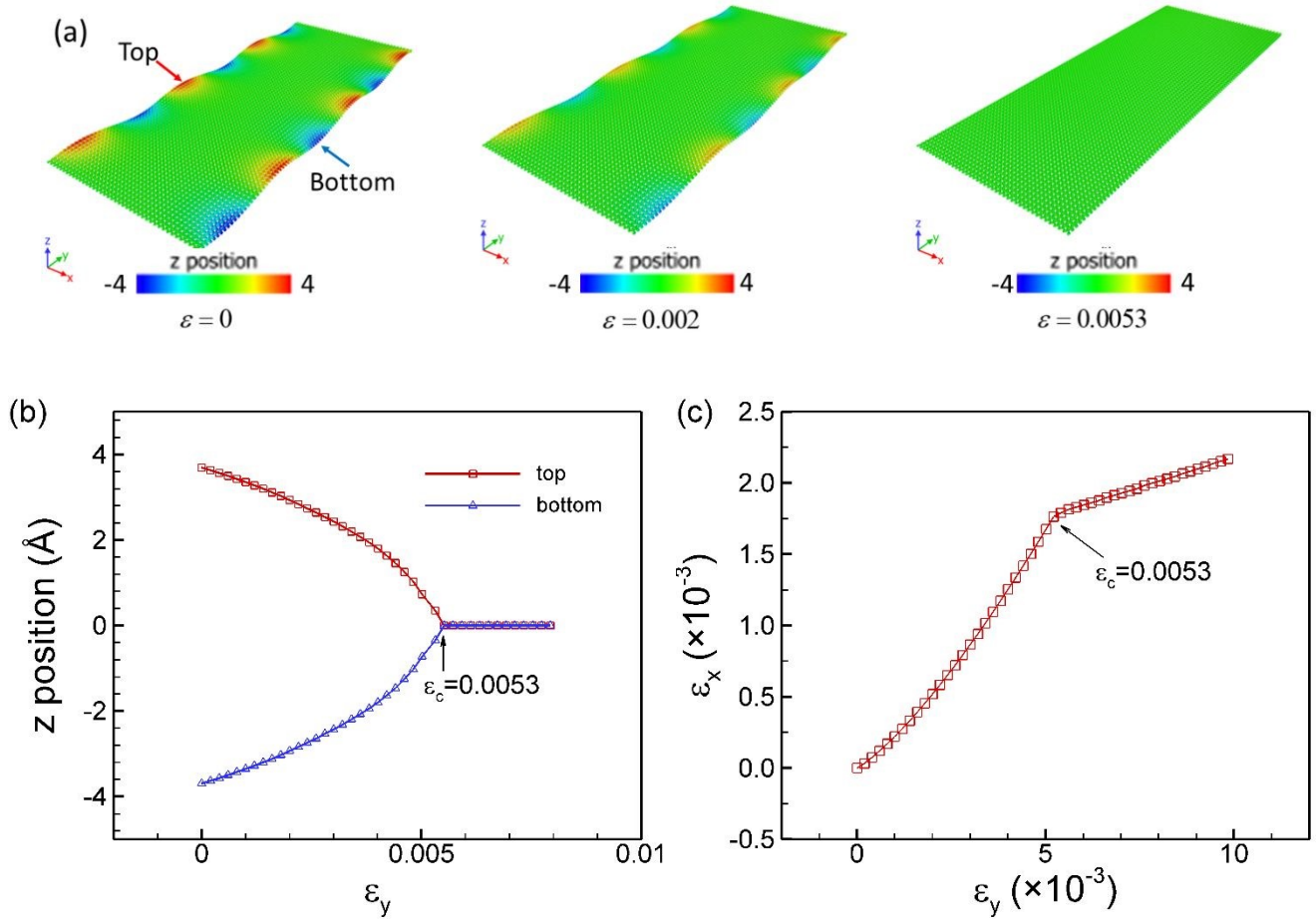

Fig. 12. (a) Snapshots of PG ribbon (143.69 Å × 359.23 Å) under tensile deformation in the y-direction. (b) The z-position of atoms at the top and bottom of the warped edge in PG under stretching. (c) Resultant strain in the x-direction under stretching in the y-direction.

Fig. 12a shows snapshots of the PG ribbon at several strains during tension in the y-direction. We found that under stretching, the configuration of warped edge is transformed from three-dimensional to two-dimensional, and the PG ribbon is completely flattened as the tensile strain excessed 0.0053. To further understand the

View Article Online
DOI: 10.1039/D2CP03275A

deformation of the warped edge, we quantified the relationship between the amplitude of the warped edges and applied strain for ribbon with width of 143.69 Å (Fig. 12b). Results clearly show that the amplitude of the warped edge reduces and becomes zero at a critical strain of $\varepsilon_c = 0.0053$, which is similar to that illustrated in Fig. 12a. This critical strain ε_c indicates a structural transformation of the warped edge. Moreover, the two deformation schemes can be clearly distinguished from the ε_x - ε_y curve shown in Fig. 12c. At a small strain $\varepsilon \leq \varepsilon_c$, the deformation of the ribbon is the combination of deformation of the warped edge at the outer part and the pristine monolayer PG at the interior part of the ribbon. The flattening of the warped edge leads to the planar expansion of ribbon; thus, it contributes to the in-plane auxeticity of the ribbon. Combined with the intrinsic negative Poisson's ratio of pristine monolayer PG in the interior regions, the ribbon may have a smaller value of in-plane Poisson's ratio (more auxeticity) than that of the former case. As the strain $\varepsilon \geq \varepsilon_c$, the configuration of ribbon is transformed into a two-dimensional planar structure, and the deformation mechanisms of ribbon are similar to those of monolayer PG, as discussed in the previous section. In Fig. 13a, we present the in-plane Poisson's ratio of PG ribbon as the structure is stretched. We only show Poisson's ratios under small strains before the structural transition occurs. It was found that the Poisson's ratio decreases with an increase of applied strain. The width dependence of the in-plane Poisson's ratio is shown in Fig. 13b. It is worthy noted that the Poisson's ratio in Fig. 13b is obtained by averaging the value of Poisson's ratio from 0 to ε_c. We realize that the Poisson's ratio increases (less negative) as the width of ribbon enhances, and the correlation of Poisson's ratio and width can be fitted to the function $\nu = -0.085 - 35.22 / w$. The PG ribbon can be separated into three regions: the interior region of ribbon and two warped edge regions. The width of each warped edge region is approximately twice the penetration depth *l*; thus, the width of the remaining interior region is $w - 4l$. Therefore, the effective Poisson's ratio of the PG ribbon can be expressed as:

$$\nu = \nu_0 + \frac{4l}{w}\left(\nu_e - \nu_0\right) \tag{7}$$

where ν_0 and ν_e are the Poisson's ratios of the interior and warped edge regions, respectively. From the fitting function and Eq.7, we obtain $\nu_0 = -0.085$ (Poisson's ratio of monolayer PG) and $\nu_e = -0.62$.

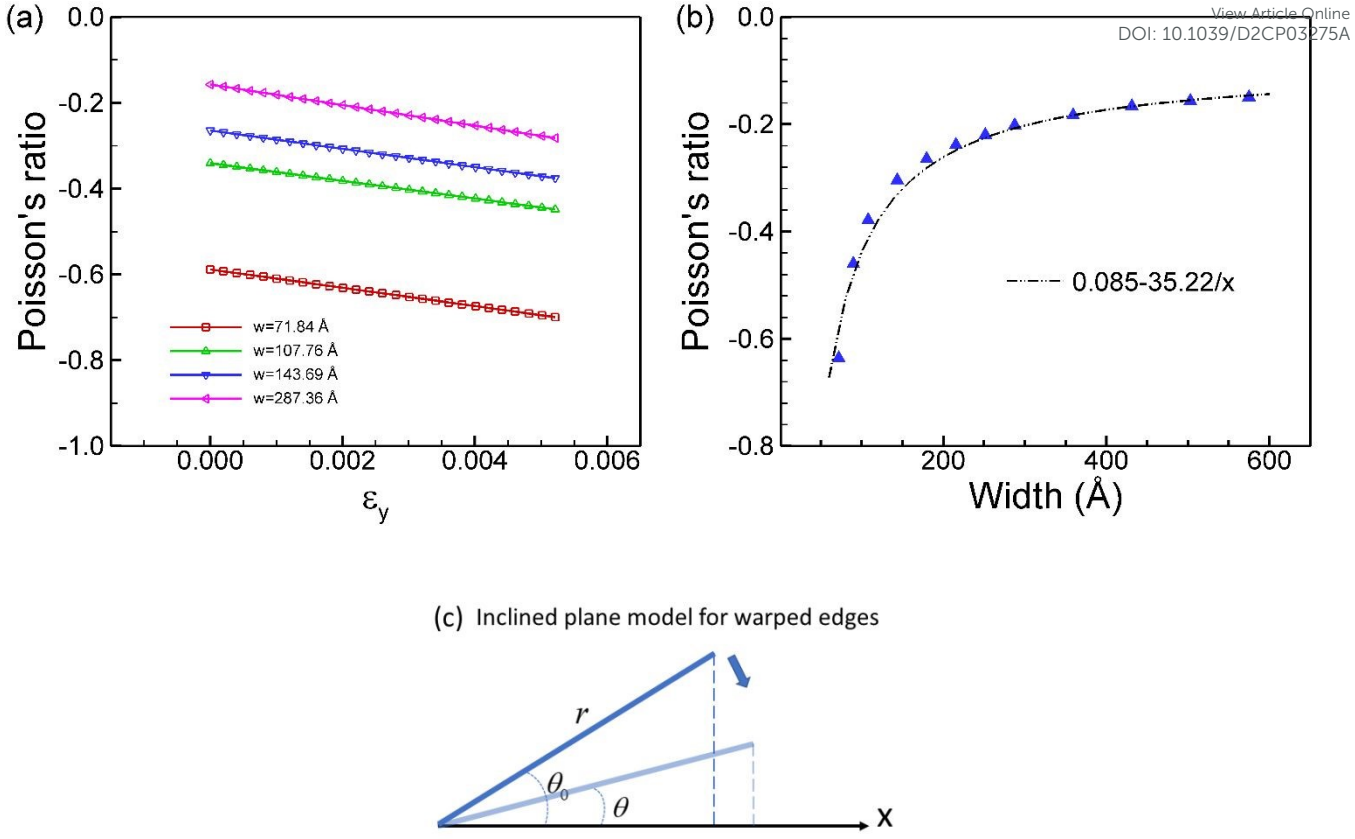

Fig. 13. (a) Relationship between the Poisson's ratio and tensile strain in the *y*-direction. The ribbon has *L*=359.23 Å, while width of ribbon is varied. (b) The dependence of in-plane Poisson's ratio on width of ribbon. (c) The analytic model to describe the warped edge, which is represented by an inclined plane (blue line).

To understand the connection between the in-plane negative Poisson's ratio and the width of PG ribbon, an analytical model of warped edge was proposed [30]. The warped edge is illustrated by an inclined plane (IP) as shown in Fig. 13c. θ is the angle between the IP and *x*-direction, and r is the length of IP. The length of IP in the *x*-direction is the value of its projection $r\cos\theta$. When the ribbon is stretched in the *y*-direction, the IP decreases, resulting in the reduction of angle θ. The strain dependence of angle θ can be expressed as:

$$\theta = \theta_0\left(1-\frac{\varepsilon}{\varepsilon_c}\right) \tag{8}$$

with θ_0 is the value of IP's angle at the unstrained configuration. When $\varepsilon = \varepsilon_0$, θ becomes zero, which represents the flattening of warped edge at the critical strain as shown in Fig. 13. The strain in the *x*-direction, corresponding to the tensile strain in the *y*-direction can be expressed as:

View Article Online
DOI: 10.1039/D2CP03275A

$$\varepsilon_x = \frac{r\cos\theta - r\cos\theta_0}{r\cos\theta_0} = \frac{\cos\theta - \cos\theta_0}{\cos\theta_0} \approx \frac{\theta_0^2}{\varepsilon_c}\varepsilon_y \tag{9}$$

Consequently, the in-plane Poisson's ratio of warped edge (ν_e) is obtained as:

$$\nu_e = -\frac{\partial\varepsilon_x}{\partial\varepsilon_y} = -\frac{\theta_0^2}{\varepsilon_c} \tag{10}$$

Assuming that the IP's angle is small, the angle with respect to the *x*-coordinate at an arbitrary point on the warped edge is given as:

$$\phi(x,y) = \tan^{-1}\left(\frac{\partial s}{\partial x}\right) \approx \frac{A}{l}e^{-x/l}\sin\frac{\pi y}{\lambda} \tag{11}$$

The IP's angle at the initial configuration θ_0 of the warped edge with $x \in [0, 2l]$ and $y \in [0, \lambda]$ can be expressed as:

$$\theta_0 = \frac{1}{2\lambda l}\int_0^{\lambda} dy \int_0^{2l} \phi(x,y)dx = \frac{A}{\pi l}\left(1 - \frac{1}{e^2}\right) \tag{12}$$

Hence, using Eq.10 the in-plane Poisson's ratio can be obtained:

$$\nu_e = -\frac{\theta_0^2}{\varepsilon_c} = -\frac{\left(\frac{A}{\pi l}\left(1 - \frac{1}{e^2}\right)\right)^2}{\varepsilon_c} \tag{13}$$

in which the amplitude of warped edge (*A*) and penetration depth (*l*) are 3.65 Å and 16.32 Å, respectively. The critical strain (ε_c) is 0.005, which is the saturation value of ε_c at width $\to \infty$ (Fig. S10 in the Supporting Information). By applying these values to Eq. 13, the in-plane Poisson's ratio of warped edge is of −0.75, which is close to the value obtained from the width dependence of Poisson's ratio (ν_e = −0.62) in Fig. 13b. Therefore, the proposed IP model can describe the in-plane Poisson's ratio of warped edge PG ribbon. It is

worth noted that as the temperature increases, the thermal-induced fluctuations may become large enough to change the warped edge configuration (Supporting Information).

View Article Online
DOI: 10.1039/D2CP03275A

4. Conclusions

In this study, we investigated the auxeticity of the monolayer, few-layer, vdW heterostructure and ribbon PG. We found that negative Poisson's ratio is the combination of the bond stretching and angle rotating deformation mechanism. Monolayer PG shows the partially auxetic behavior (i.e., negative in-plane and positive out-of-plane Poisson's ratio). The dominance of the bond stretching mechanism results in a negative in-plane Poisson's ratio in monolayer PG. The angle rotation mechanism significantly increases the in-plane Poisson's ratio of few-layer PG and enables it to turn to positive values. The elongation of interlayer bonds is found to be the origin of auxeticity in the out-of-plane direction of few-layer PG. Moreover, the strong dependence of Poisson's ratio on the stacking configuration and number of layers was also observed. We also demonstrate the minor effect of vdW interaction on the auxeticity of heterostructure PG. Finally, we found the significant effect of warped edge on the in-plane auxeticity of PG ribbon. We expect our results can provide a further explanation of the mechanism for low-dimensional materials with intrinsic auxeticity rather than extrinsic auxeticity, which requires a complex structural design of the materials.

Author contribution

Viet Hung Ho wrote the manuscript and discussed with Duc Tam Ho and Won Ho Shin. Sung Youb Kim supervised the project.

View Article Online
DOI: 10.1039/D2CP03275A

Conflict of interest

The author declares no competing financial or non-financial interests.

Acknowledgments

We gratefully acknowledge the support from the Basic Research Laboratory Support Program (Grant No. 2021R1A4A1033224) of the National Research Foundation of Korea funded by the Korean government (MSIT). We also acknowledge with gratitude the supercomputing resources of the UNIST Supercomputing Center.

Reference

(1) Evans, K. E.; Nkansah, M. A.; Hutchinson, I. J.; Rogers, S. C. Molecular Network Design. *Nature* **1991**, *353* (6340), 124–124. https://doi.org/10.1038/353124a0.

(2) Lakes, R. Foam Structures with a Negative Poisson's Ratio. *Science* **1987**, *235* (4792), 1038–1040. https://doi.org/10.1126/science.235.4792.1038.

(3) Lakes, R. Negative Poisson's Ratio Materials. *Science* **1987**, *238* (4826), 551–551. https://doi.org/10.1126/science.238.4826.551.a.

(4) Wojciechowski, K. W. Two-Dimensional Isotropic System with a Negative Poisson Ratio. *Phys. Lett. A* **1989**, *137* (1), 60–64. https://doi.org/10.1016/0375-9601(89)90971-7.

(5) Wojciechowski, K. W. Constant Thermodynamic Tension Monte Carlo Studies of Elastic Properties of a Two-Dimensional System of Hard Cyclic Hexamers. *Mol. Phys.* **1987**, *61* (5), 1247–1258. https://doi.org/10.1080/00268978700101761.

(6) Choi, J. B.; Lakes, R. S. Fracture Toughness of Re-Entrant Foam Materials with a Negative Poisson's Ratio: Experiment and Analysis. *Int. J. Fract.* **1996**, *80* (1), 73–83. https://doi.org/10.1007/BF00036481.

(7) Alderson, A.; Alderson, K. L. Auxetic Materials. *Proc. Inst. Mech. Eng. Part G J. Aerosp. Eng.* **2007**, *221* (4), 565–575. https://doi.org/10.1243/09544100JAERO185.

(8) Liu, Y.; Hu, H.; Lam, J. K. C.; Liu, S. Negative Poisson's Ratio Weft-Knitted Fabrics. *Text. Res. J.* **2010**, *80* (9), 856–863. https://doi.org/10.1177/0040517509349788.

(9) Jang, K.-I.; Chung, H. U.; Xu, S.; Lee, C. H.; Luan, H.; Jeong, J.; Cheng, H.; Kim, G.-T.; Han, S. Y.; Lee, J. W.; Kim, J.; Cho, M.; Miao, F.; Yang, Y.; Jung, H. N.; Flavin, M.; Liu, H.; Kong, G. W.; Yu, K. J.; Rhee, S. I.; Chung, J.; Kim, B.; Kwak, J. W.; Yun, M. H.; Kim, J. Y.; Song, Y. M.; Paik, U.; Zhang, Y.; Huang, Y.; Rogers, J. A. Soft Network Composite Materials with Deterministic and Bio-Inspired Designs. *Nat. Commun.* **2015**, *6* (1), 6566. https://doi.org/10.1038/ncomms7566.

(10) Jiang, Y.; Liu, Z.; Matsuhisa, N.; Qi, D.; Leow, W. R.; Yang, H.; Yu, J.; Chen, G.; Liu, Y.; Wan, C.; Liu, Z.; Chen, X. Auxetic Mechanical Metamaterials to Enhance Sensitivity of Stretchable Strain Sensors. *Adv. Mater.* **2018**, *30* (12), 1706589. https://doi.org/10.1002/adma.201706589.

(11) Lim, T.-C. *Auxetic Materials and Structures*; Engineering Materials; Springer Singapore, 2015. https://doi.org/10.1007/978-981-287-275-3.

(12) Kim, B. S.; Lee, K.; Kang, S.; Lee, S.; Pyo, J. B.; Choi, I. S.; Char, K.; Park, J. H.; Lee, S.-S.; Lee, J.; Son, J. G. 2D Reentrant Auxetic Structures of Graphene/CNT Networks for Omnidirectionally Stretchable Supercapacitors. *Nanoscale* **2017**, *9* (35), 13272–13280. https://doi.org/10.1039/C7NR02869E.

(13) Jiang, Y.; Li, Y. 3D Printed Auxetic Mechanical Metamaterial with Chiral Cells and Re-Entrant Cores. *Sci. Rep.* **2018**, *8* (1), 1–11. https://doi.org/10.1038/s41598-018-20795-2.

(14) Grima, J. N.; Alderson, A.; Evans, K. E. Auxetic Behaviour from Rotating Rigid Units. *Phys. Status Solidi B* **2005**, *242* (3), 561–575. https://doi.org/10.1002/pssb.200460376.

(15) Rossiter, J.; Takashima, K.; Scarpa, F.; Walters, P.; Mukai, T. Shape Memory Polymer Hexachiral Auxetic Structures with Tunable Stiffness. *Smart Mater. Struct.* **2014**, *23* (4), 045007. https://doi.org/10.1088/0964-1726/23/4/045007.

(16) Schenk, M.; Guest, S. D. Geometry of Miura-Folded Metamaterials. *Proc. Natl. Acad. Sci.* **2013**, *110* (9), 3276–3281. https://doi.org/10.1073/pnas.1217998110.

(17) Yasuda, H.; Yang, J. Reentrant Origami-Based Metamaterials with Negative Poisson's Ratio and Bistability. *Phys. Rev. Lett.* **2015**, *114* (18), 185502. https://doi.org/10.1103/PhysRevLett.114.185502.

(18) Rothenburg, L.; AI. Berlin, A. I.; Bathurst, R. J. Microstructure of Isotropic Materials with Negative Poisson's Ratio. *Nature* **1991**, *354* (6353), 470–472. https://doi.org/10.1038/354470a0.

(19) Guo, S.; Sun, H. Manipulation of Giant Negative Poisson's Ratios in Three-Dimensional Graphene Networks. *Phys. Rev. B* **2020**, *102* (18), 184116. https://doi.org/10.1103/PhysRevB.102.184116.

(20) Nguyen, C. T.; Ho, D. T.; Choi, S. T.; Chun, D.-M.; Kim, S. Y. Pattern Transformation Induced by Elastic Instability of Metallic Porous Structures. *Comput. Mater. Sci.* **2019**, *157*, 17–24. https://doi.org/10.1016/j.commatsci.2018.10.023.

(21) Reid, D. R.; Pashine, N.; Wozniak, J. M.; Jaeger, H. M.; Liu, A. J.; Nagel, S. R.; Pablo, J. J. de. Auxetic Metamaterials from Disordered Networks. *Proc. Natl. Acad. Sci.* **2018**, *115* (7), E1384–E1390. https://doi.org/10.1073/pnas.1717442115.

(22) Wojciechowski, K. W. Non-Chiral, Molecular Model of Negative Poisson Ratio in Two Dimensions. *J. Phys. Math. Gen.* **2003**, *36* (47), 11765. https://doi.org/10.1088/0305-4470/36/47/005.

(23) Lakes, R.; Wojciechowski, K. W. Negative Compressibility, Negative Poisson's Ratio, and Stability. *Phys. Status Solidi B* **2008**, *245* (3), 545–551. https://doi.org/10.1002/pssb.200777708.

(24) Ho, D. T.; Park, S.-D.; Kwon, S.-Y.; Park, K.; Kim, S. Y. Negative Poisson's Ratios in Metal Nanoplates. *Nat. Commun.* **2014**, *5* (1), 3255. https://doi.org/10.1038/ncomms4255.

(25) Ho, D. T.; Kwon, S.-Y.; Kim, S. Y. Metal [100] Nanowires with Negative Poisson's Ratio. *Sci. Rep.* **2016**, *6*, 27560. https://doi.org/10.1038/srep27560.

(26) Grima, J. N.; Winczewski, S.; Mizzi, L.; Grech, M. C.; Cauchi, R.; Gatt, R.; Attard, D.; Wojciechowski, K. W.; Rybicki, J. Tailoring Graphene to Achieve Negative Poisson's Ratio Properties. *Adv. Mater.* **2015**, *27* (8), 1455–1459. https://doi.org/10.1002/adma.201404106.

(27) Ho, V. H.; Ho, D. T.; Kwon, S.-Y.; Kim, S. Y. Negative Poisson's Ratio in Periodic Porous Graphene Structures. *Phys. Status Solidi B* **2016**, *253* (7), 1303–1309. https://doi.org/10.1002/pssb.201600061.

(28) Jiang, J.-W.; Chang, T.; Guo, X. Tunable Negative Poisson's Ratio in Hydrogenated Graphene. *Nanoscale* **2016**, *8* (35), 15948–15953. https://doi.org/10.1039/C6NR04976A.

(29) Wan, J.; Jiang, J.-W.; Park, H. S. Negative Poisson's Ratio in Graphene Oxide. *Nanoscale* **2017**, *9* (11), 4007–4012. https://doi.org/10.1039/C6NR08657H.

(30) Jiang, J.-W.; Park, H. S. Negative Poisson's Ratio in Single-Layer Graphene Ribbons. *Nano Lett.* **2016**, *16* (4), 2657–2662. https://doi.org/10.1021/acs.nanolett.6b00311.

(31) Ho, D. T.; Ho, V. H.; Babar, V.; Kim, S. Y.; Schwingenschlögl, U. Complex Three-Dimensional Graphene Structures Driven by Surface Functionalization. *Nanoscale* **2020**, *12* (18), 10172–10179. https://doi.org/10.1039/D0NR01733G.

(32) Ho, D. T.; Kim, S. Y.; Schwingenschlögl, U. Graphene Origami Structures with Superflexibility and Highly Tunable Auxeticity. *Phys. Rev. B* **2020**, *102* (17), 174106. https://doi.org/10.1103/PhysRevB.102.174106.

(33) Jiang, J.-W.; Chang, T.; Guo, X.; Park, H. S. Intrinsic Negative Poisson's Ratio for Single-Layer Graphene. *Nano Lett.* **2016**, *16* (8), 5286–5290. https://doi.org/10.1021/acs.nanolett.6b02538.

(34) Jiang, J.-W.; Park, H. S. Negative Poisson's Ratio in Single-Layer Black Phosphorus. *Nat. Commun.* **2014**, *5*, 4727. https://doi.org/10.1038/ncomms5727.

(35) Ho, D. T.; Ho, V. H.; Park, H. S.; Kim, S. Y. Negative In-Plane Poisson's Ratio for Single Layer Black Phosphorus: An Atomistic Simulation Study. *Phys. Status Solidi B* **2017**, *254* (12), 1700285. https://doi.org/10.1002/pssb.201700285.

(36) Du, Y.; Maassen, J.; Wu, W.; Luo, Z.; Xu, X.; Ye, P. D. Auxetic Black Phosphorus: A 2D Material with Negative Poisson's Ratio. *Nano Lett.* **2016**, *16* (10), 6701–6708. https://doi.org/10.1021/acs.nanolett.6b03607.

(37) Kou, L.; Ma, Y.; Tang, C.; Sun, Z.; Du, A.; Chen, C. Auxetic and Ferroelastic Borophane: A Novel 2D Material with Negative Possion's Ratio and Switchable Dirac Transport Channels. *Nano Lett.* **2016**, *16* (12), 7910–7914. https://doi.org/10.1021/acs.nanolett.6b04180.

(38) Yu, L.; Yan, Q.; Ruzsinszky, A. Negative Poisson's Ratio in 1T-Type Crystalline Two-Dimensional Transition Metal Dichalcogenides. *Nat. Commun.* **2017**, *8* (1), 15224. https://doi.org/10.1038/ncomms15224.

(39) Wang, H.; Li, X.; Li, P.; Yang, J. δ-Phosphorene: A Two Dimensional Material with a Highly Negative Poisson's Ratio. *Nanoscale* **2017**, *9* (2), 850–855. https://doi.org/10.1039/C6NR08550D.

(40) Ho, V. H.; Ho, D. T.; Nguyen, C. T.; Kim, S. Y. Negative Out-of-Plane Poisson's Ratio of Bilayer Graphane. *Nanotechnology* **2022**, *33* (25), 255705. https://doi.org/10.1088/1361-6528/ac5da0.

(41) Pan, J.; Zhang, Y.-F.; Zhang, J.; Banjade, H.; Yu, J.; Yu, L.; Du, S.; Ruzsinszky, A.; Hu, Z.; Yan, Q. Auxetic Two-Dimensional Transition Metal Selenides and Halides. *Npj Comput. Mater.* **2020**, *6* (1), 1–6. https://doi.org/10.1038/s41524-020-00424-1.

(42) Liu, X.; Shao, X.; Yang, B.; Zhao, M. Negative Poisson's Ratio and High-Mobility Transport Anisotropy in SiC6 Siligraphene. *Nanoscale* **2018**, *10* (4), 2108–2114. https://doi.org/10.1039/C7NR06932D.

(43) Li, X.; Huang, C.; Hu, S.; Deng, B.; Chen, Z.; Han, W.; Chen, L. Negative and Near-Zero Poisson's Ratios in 2D Graphene/MoS_2 and Graphene/h-BN Heterostructures. *J. Mater. Chem. C* **2020**, *8* (12), 4021–4029. https://doi.org/10.1039/C9TC06424A.

(44) Ho, V. H.; Nguyen, C. T.; Nguyen, H. D.; Oh, H. S.; Shin, M.; Kim, S. Y. Hydrogenated Graphene with Tunable Poisson's Ratio Using Machine Learning: Implication for Wearable Devices and Strain Sensors. *ACS Appl. Nano Mater.* **2022**, *5* (8), 10617–10627. https://doi.org/10.1021/acsanm.2c01950.

(45) Zhang, S.; Zhou, J.; Wang, Q.; Chen, X.; Kawazoe, Y.; Jena, P. Penta-Graphene: A New Carbon Allotrope. *Proc. Natl. Acad. Sci.* **2015**, *112* (8), 2372–2377. https://doi.org/10.1073/pnas.1416591112.

(46) Wang, Z.; Dong, F.; Shen, B.; Zhang, R. J.; Zheng, Y. X.; Chen, L. Y.; Wang, S. Y.; Wang, C. Z.; Ho, K. M.; Fan, Y.-J.; Jin, B.-Y.; Su, W.-S. Electronic and Optical Properties of Novel Carbon Allotropes. *Carbon* **2016**, *101*, 77–85. https://doi.org/10.1016/j.carbon.2016.01.078.

(47) Yagmurcukardes, M.; Sahin, H.; Kang, J.; Torun, E.; Peeters, F. M.; Senger, R. T. Pentagonal Monolayer Crystals of Carbon, Boron Nitride, and Silver Azide. *J. Appl. Phys.* **2015**, *118* (10), 104303. https://doi.org/10.1063/1.4930086.

(48) Yu, Z. G.; Zhang, Y.-W. A Comparative Density Functional Study on Electrical Properties of Layered Penta-Graphene. *J. Appl. Phys.* **2015**, *118* (16), 165706. https://doi.org/10.1063/1.4934855.

(49) Wang, J.; Wang, Z.; Zhang, R. J.; Zheng, Y. X.; Chen, L. Y.; Wang, S. Y.; Tsoo, C.-C.; Huang, H.-J.; Su, W.-S. A First-Principles Study of the Electrically Tunable Band Gap in Few-Layer Penta-Graphene. *Phys. Chem. Chem. Phys.* **2018**, *20* (26), 18110–18116. https://doi.org/10.1039/C8CP02624F.

(50) Li, L.; Jin, K.; Du, C.; Liu, X. The Effect of Oxidation on the Electronic Properties of Penta-Graphene: First-Principles Calculation. *RSC Adv.* **2019**, *9* (15), 8253–8261. https://doi.org/10.1039/C9RA00275H.

(51) Berdiyorov, G. R.; Dixit, G.; Madjet, M. E. Band Gap Engineering in Penta-Graphene by Substitutional Doping: First-Principles Calculations. *J. Phys. Condens. Matter* **2016**, *28* (47), 475001. https://doi.org/10.1088/0953-8984/28/47/475001.

(52) Manjanath, A.; Hsu, C.-P.; Kawazoe, Y. Tuning the Electronic and Magnetic Properties of Pentagraphene through the C1 Vacancy. *2D Mater.* **2020**, *7* (4), 045024. https://doi.org/10.1088/2053-1583/aba565.

(53) Berdiyorov, G. R.; Madjet, M. E.-A. First-Principles Study of Electronic Transport and Optical Properties of Penta-Graphene, Penta-SiC2 and Penta-CN2. *RSC Adv.* **2016**, *6* (56), 50867–50873. https://doi.org/10.1039/C6RA10376F.

(54) Xiao, B.; Li, Y.; Yu, X.; Cheng, J. Penta-Graphene: A Promising Anode Material as the Li/Na-Ion Battery with Both Extremely High Theoretical Capacity and Fast Charge/Discharge Rate. *ACS Appl. Mater. Interfaces* **2016**, *8* (51), 35342–35352. https://doi.org/10.1021/acsami.6b12727.

(55) Krishnan, R.; Su, W.-S.; Chen, H.-T. A New Carbon Allotrope: Penta-Graphene as a Metal-Free Catalyst for CO Oxidation. *Carbon* **2017**, *114*, 465–472. https://doi.org/10.1016/j.carbon.2016.12.054.

(56) Wang, M.; Zhang, Z.; Gong, Y.; Zhou, S.; Wang, J.; Wang, Z.; Wei, S.; Guo, W.; Lu, X. Penta-Graphene as a Promising Controllable CO2 Capture and Separation Material in an Electric Field. *Appl. Surf. Sci.* **2020**, *502*, 144067. https://doi.org/10.1016/j.apsusc.2019.144067.

(57) Sun, H.; Mukherjee, S.; Singh, C. V. Mechanical Properties of Monolayer Penta-Graphene and Phagraphene: A First-Principles Study. *Phys. Chem. Chem. Phys.* **2016**, *18* (38), 26736–26742. https://doi.org/10.1039/C6CP04595B.

(58) Winczewski, S.; Rybicki, J. Anisotropic Mechanical Behavior and Auxeticity of Penta-Graphene: Molecular Statics/Molecular Dynamics Studies. *Carbon* **2019**, *146*, 572–587. https://doi.org/10.1016/j.carbon.2019.02.042.

(59) Lee, C.; Wei, X.; Kysar, J. W.; Hone, J. Measurement of the Elastic Properties and Intrinsic Strength of Monolayer Graphene. *Science* **2008**, *321* (5887), 385–388. https://doi.org/10.1126/science.1157996.

(60) Xu, W.; Zhang, G.; Li, B. Thermal Conductivity of Penta-Graphene from Molecular Dynamics Study. *J. Chem. Phys.* **2015**, *143* (15), 154703. https://doi.org/10.1063/1.4933311.

(61) Wang, F. Q.; Yu, J.; Wang, Q.; Kawazoe, Y.; Jena, P. Lattice Thermal Conductivity of Penta-Graphene. *Carbon* **2016**, *105*, 424–429. https://doi.org/10.1016/j.carbon.2016.04.054.

(62) Balandin, A. A. Thermal Properties of Graphene and Nanostructured Carbon Materials. *Nat. Mater.* **2011**, *10* (8), 569–581. https://doi.org/10.1038/nmat3064.

(63) Winczewski, S.; Shaheen, M. Y.; Rybicki, J. Interatomic Potential Suitable for the Modeling of Penta-Graphene: Molecular Statics/Molecular Dynamics Studies. *Carbon* **2018**, *126*, 165–175. https://doi.org/10.1016/j.carbon.2017.10.002.

(64) Erhart, P.; Albe, K. Analytical Potential for Atomistic Simulations of Silicon, Carbon, and Silicon Carbide. *Phys. Rev. B* **2005**, *71* (3), 035211. https://doi.org/10.1103/PhysRevB.71.035211.

(65) Polak, E.; Ribiere, G. Note sur la convergence de méthodes de directions conjuguées. *Rev. Fr. Inform. Rech. Opérationnelle Sér. Rouge* **1969**, *3* (16), 35–43. https://doi.org/10.1051/m2an/196903R100351.

(66) Plimpton, S. Fast Parallel Algorithms for Short-Range Molecular Dynamics. *J. Comput. Phys.* **1995**, *117* (1), 1–19. https://doi.org/10.1006/jcph.1995.1039.

(67) Stukowski, A. Visualization and Analysis of Atomistic Simulation Data with OVITO–the Open Visualization Tool. *Model. Simul. Mater. Sci. Eng.* **2009**, *18* (1), 015012. https://doi.org/10.1088/0965-0393/18/1/015012.

(68) Chang, T.; Gao, H. Size-Dependent Elastic Properties of a Single-Walled Carbon Nanotube via a Molecular Mechanics Model. *J. Mech. Phys. Solids* **2003**, *51* (6), 1059–1074. https://doi.org/10.1016/S0022-5096(03)00006-1.

(69) Hu, Y.; Chen, J.; Wang, B. On the Intrinsic Ripples and Negative Thermal Expansion of Graphene. *Carbon* **2015**, *95*, 239–249. https://doi.org/10.1016/j.carbon.2015.08.022.

(70) Sajadi, B.; van Hemert, S.; Arash, B.; Belardinelli, P.; Steeneken, P. G.; Alijani, F. Size- and Temperature-Dependent Bending Rigidity of Graphene Using Modal Analysis. *Carbon* **2018**, *139*, 334–341. https://doi.org/10.1016/j.carbon.2018.06.066.

(71) Zhao, K.; Guo, Y.; Wang, Q. Contact Properties of a VdW Heterostructure Composed of Penta-Graphene and Penta-BN_2 Sheets. *J. Appl. Phys.* **2018**, *124* (16), 165103. https://doi.org/10.1063/1.5047539.

(72) Chen, X.; Zhang, L.; Park, C.; Fay, C. C.; Wang, X.; Ke, C. Mechanical Strength of Boron Nitride Nanotube-Polymer Interfaces. *Appl. Phys. Lett.* **2015**, *107* (25), 253105. https://doi.org/10.1063/1.4936755.

(73) Shenoy, V. B.; Reddy, C. D.; Ramasubramaniam, A.; Zhang, Y. W. Edge-Stress-Induced Warping of Graphene Sheets and Nanoribbons. *Phys. Rev. Lett.* **2008**, *101* (24), 245501. https://doi.org/10.1103/PhysRevLett.101.245501.

(74) Bets, K. V.; Yakobson, B. I. Spontaneous Twist and Intrinsic Instabilities of Pristine Graphene Nanoribbons. *Nano Res.* **2009**, *2* (2), 161–166. https://doi.org/10.1007/s12274-009-9015-x.

(75) Shenoy, V. B.; Reddy, C. D.; Zhang, Y.-W. Spontaneous Curling of Graphene Sheets with Reconstructed Edges. *ACS Nano* **2010**, *4* (8), 4840–4844. https://doi.org/10.1021/nn100842k.